Cold Regions Science and Technology 228 (2024) 104325

Contents lists available at ScienceDirect

Cold Regions Science and Technology

journal homepage: www.elsevier.com/locate/coldregions

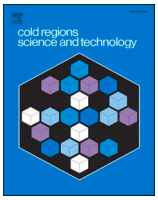

Evaluating the importance of footloose-type failure in ice island deterioration modeling

Anna J. Crawford [a,b,*], Greg Crocker [c], Jesse Smith [c], Derek Mueller [c], Till J.W. Wagner [d]

[a] Division of Biological and Environmental Sciences, University of Stirling, Stirling FK9 4LA, UK
[b] School of GeoSciences, University of Edinburgh, Edinburgh EH8 9XP, UK
[c] Department of Geography and Environmental Studies, Carleton University, Ottawa K1S 5B6, Canada
[d] Department of Atmospheric and Oceanic Sciences, University of Wisconsin-Madison, Madison, WI 53706, USA

ARTICLE INFO

Keywords:
Iceberg
Ice island
Calving
Deterioration
Ice fracture

ABSTRACT

The drift and deterioration of large and tabular icebergs, also known as “ice islands” in the Arctic, are modeled for both operational (e.g., offshore risk mitigation) and research (e.g., oceanographic impact of melt water input) purposes. In this paper, we build a theoretical argument to show that the lateral deterioration of ice islands is controlled by the rate of sidewall notch growth at the waterline, with this growth leading to the development of underwater rams and buoyancy-induced calving via the ‘footloose’ mechanism. This dominance of footloose-type lateral deterioration allows for the majority of ice island deterioration to be simulated with only three oceanic variables: wave height, wave period, and sea-surface temperature. Information regarding the size and lineage of ice islands tracked in the Canadian Ice Island Drift, Deterioration and Detection (CI2D3) Database provides opportunity to assess our theoretical work, as the database serves as a validation dataset for simulations of ice island length and area change. When simulating the length reduction over time of ice islands tracked in the CI2D3 Database, the footloose model reduced the mean error over 80 d to +277 m, compared to −1545 and −1403 m with no-melt and thermal-melt models, respectively. We also demonstrate a new approach to simulating the areal deterioration of ice islands resulting from discrete footloose calving events. The approach utilizes two parameters: the length-to-width ratio of the ice island (r) and the width of a footloose calving event relative to the ice island’s length (K). With $r = 1.6$ and $K = 0.8$, the mean error in modeled area was close to zero after 20 d of simulation. A comparison of stresses associated with footloose events from a 1D-beam model and those simulated with 3D finite-element modeling showed that the 1D and 3D simulations produce broadly similar results. This supports our approaches and parameter assignments for simulating ice island length and area reduction from footloose calving. These approaches can now be incorporated into ice island deterioration models. The benefit of this incorporation will be greatest for those interested in research of longer-term impacts of ice island deterioration on ocean properties given the greater improvements to model error over periods of time that are longer than those that usually concern offshore ice management operations.

1. Introduction

Large tabular icebergs calve from ice shelves and ice tongues in both the Northern and Southern hemispheres. These “ice islands”, as they are referred to in the Northern Hemisphere, drift away from their source glaciers and deteriorate through both thermal and mechanical processes. Ice islands in the Arctic can range in size from a few thousand square meters to several hundred square kilometers (Canadian Ice Service, 2005), while Antarctic ice islands can reach thousands of square kilometers in size. We use the term “iceberg” when it is appropriate to refer to ice islands, tabular icebergs and other, non-tabular icebergs together.

Although ultimate ice decay is thermal, intermittent mechanical processes (fracture) can hasten the deterioration of icebergs by increasing the surface area exposed to the atmosphere or ocean water. Government agencies (e.g., the North American Ice Service (NAIS), which is composed of the Canadian Ice Service (CIS) of Environment and Climate Change Canada (ECCC), the International Ice Patrol (IIP) of the U.S. National Oceanic and Atmospheric Administration and the U.S. National Ice Center) and private industry use models of drift and

* Corresponding author at: Division of Biological and Environmental Sciences, University of Stirling, Stirling FK9 4LA, UK.
E-mail address: anna.crawford@stir.ac.uk (A.J. Crawford).

https://doi.org/10.1016/j.coldregions.2024.104325
Received 5 July 2023; Received in revised form 9 July 2024; Accepted 16 September 2024
Available online 17 September 2024

deterioration to produce ice hazard spatial density products (Fuglem et al., 2012; Kubat et al., 2005). These products are valuable for the offshore hydrocarbon and other industries in facility design and operationally as part of their alert systems (Fuglem and Jordaan, 2017; Turnbull et al., 2015). Drift and deterioration models are also used in scientific studies, for example, to investigate the variation in spatial and temporal distribution of freshwater delivered to the ocean and the resulting effects on Meridional Overturning Circulation (Crawford et al., 2015, 2018b, 2020; Marson et al., 2021) or the impact on sea-ice distributions (Merino et al., 2016).

Models of thermo-mechanical decay vary in complexity. Some address melt at the base and sides of icebergs (Bigg et al., 1997; Crawford et al., 2020; Gladstone et al., 2001; Weeks and Campbell, 1973; White et al., 1980), and some attempt to capture several melt processes in one or more semi-empirical expressions (Bigg et al., 1997; England et al., 2020; Gladstone et al., 2001; Martin et al., 1978). White et al. (1980) attempted to identify all the important processes contributing to melt and model each process explicitly. These formulations are used in the iceberg drift and deterioration models of NAIS, which is applied at the CIS (Kubat et al., 2007; Motz, 2022).

Ice islands can be regarded as thin sheets that have much greater perimeter to volume ratios than non-tabular icebergs. This leads to the possibility of fracture processes playing a larger role in the overall deterioration of ice islands. The White et al. (1980) model includes a calving component that accounts for fracture and removal of ice above a wave notch, which forms at the waterline where high orbital velocities and wave breaking lead to enhanced heat transfer. The weight of the material in the overhanging ice causes shear stresses at the root of the notch and tensile stresses at the upper surface that eventually exceed ice strength and lead to the collapse of the overhang, akin to serac failure of tidewater glaciers. The removal of ice above but not below the notch leads to the formation of an underwater "ram" or "foot", which is a lateral extension of ice below the waterline (Figs. 1b, 2).

Stresses associated with these rams can lead to large scale fracture of ice islands and greatly enhanced overall deterioration rates. Crocker (2012) postulated that because very large underwater rams are quite rare, the ice making up a ram must eventually be removed by some mechanical calving process. Crocker et al. (2013) noted that accurate models of ice island deterioration would only be achieved when large-scale fracture was incorporated, but they did not elaborate on precisely what the mechanical processes might be. In the present study, we use White et al.'s (1980) formulations for wave erosion to drive a model of mechanical fracture that is based on Wagner et al.'s (2014) "footloose" calving mechanism. This calving, associated with ram formation, leads to "edge-wasting" type deterioration where edge-parallel calving gradually reduces the lateral dimensions of an ice island (Scambos et al., 2005). We then evaluate the applicability of the 1D-fracture model to ice island deterioration modeling through two analyses. First, we compare hindcasts of length and area reductions to observations of ice island deterioration extracted from the Canadian Ice Island Drift, Deterioration and Detection (CI2D3) Database (Crawford et al., 2018a), a data repository associated with ice islands that calved from northwest Greenland between 2008 and 2013. In the second analysis, we look at the 3D stress fields for a subset of ice islands in the CI2D3 Database that were identified to have undergone footloose calving to compare the stresses corresponding with the 1D and 3D modeling approaches and investigate how the higher dimensions may impact footloose calving.

2. Background

One of the first investigations into large-scale fracture of icebergs was performed by Goodman et al. (1980), who analyzed stresses and fracture resulting from long-period gravity waves. Diemand (1987) looked at iceberg splitting due to buoyant forces created by the formation of underwater rams (Figs. 1b, 2). Although calving failure of iceberg rams had been observed (Hodgson et al., 1988), it was not known how common this was.

If the rams calved at the wave notch it would mean that the long-term lateral erosion of an ice island exposed to ocean swell would be entirely dependent on, and equal to, the rate at which the wave notch grows. Diemand (1987) and Hodgson et al. (1988) reported two instances in which calving indeed occurred at the position of the wave notch. However, these were large icebergs, and their irregular shapes and limited extent when compared to ice islands may have been factors

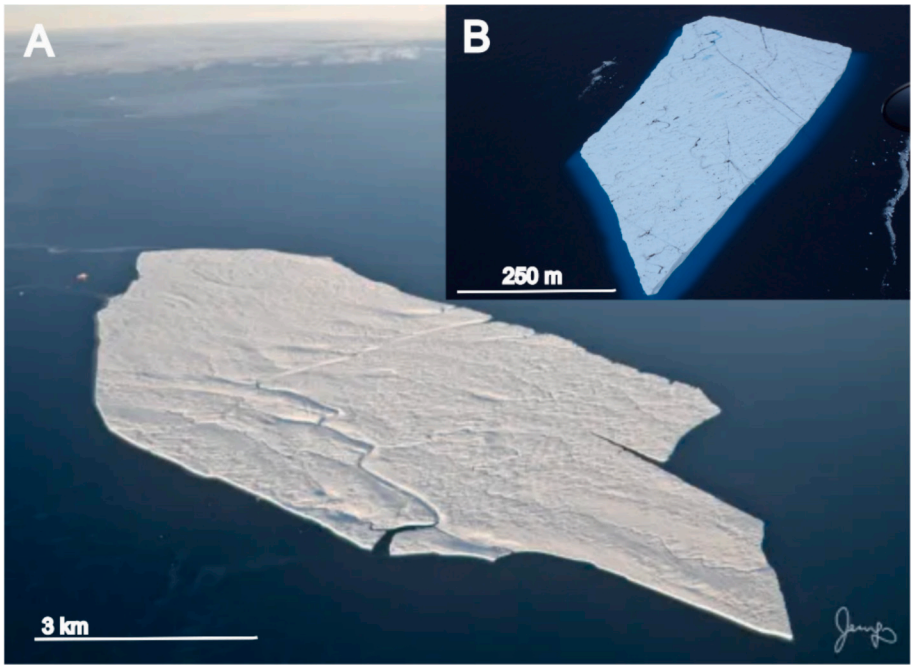

Fig. 1. (A) An aerial view of an ice island in Lancaster Sound, Nunavut, Canada. Image courtesy of Jesse Barrette. (B) The underwater ram of Berghaus, an ice island fragment in Lancaster Sound is seen as the lighter, turquoise color. (For interpretation of the references to color in this figure legend, the reader is referred to the web version of this article.)

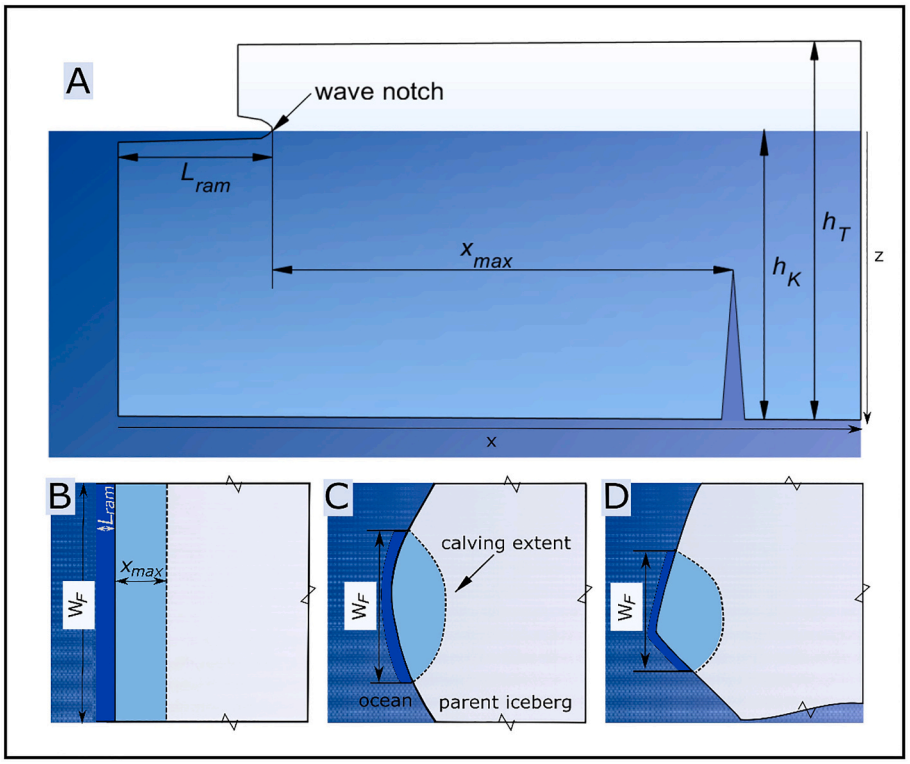

Fig. 2. Side view (A) and planar (B-D) geometries showing example scenarios of calving via the footloose mechanism. The ice within the region demarcated by the calving extent (noted in C) will become a child fragment of the parent ice island if it remains intact post-calving. Nomenclature used in the analysis and included in (A) is W_F = failure width, L_{ram} = ram length, x_{max} = location of greatest stress and distance from wave notch to point of failure, h_k = ice island keel depth, h_T = ice island total thickness, z = depth below waterline. Failure will occur at point x_{max} when $L_{ram} = L_{crit}$, with L_{crit} being the critical ram length at which failure will occur.

in concentrating stresses near the notch. Wagner et al. (2014) showed that stresses due to the presence of a ram typically reach maximum values at a location further into the interior of the ice island than the notch itself. Wagner et al. (2014) applied elastic beam theory to estimate bending and fracture due to buoyant forces arising from these underwater rams. This demonstrated that the rate of lateral erosion can be much greater than the rate of notch growth. It was found the model could replicate footloose failure observed at “Petermann Ice Island-B" in western Baffin Bay if the strength threshold for tensile failure was reduced to a low value of 100 kPa (Crawford et al., 2016; Wagner et al., 2014). A schematic of the ram geometry associated with the footloose mechanism is provided in Fig. 2A. We illustrate three possible footloose calving geometries in Fig. 2 (B–D).

It has been argued that the footloose-calving process can be a significant contributor to the overall decay rate of an ice island (Wagner et al., 2014) as well as for tidewater glaciers (Wagner et al., 2016) and ice shelves (Becker et al., 2021; Sartore et al., 2024). While the work of Wagner et al. (2014) is limited to a 1-dimensional beam analysis, the footloose fracture process is inherently 3-dimensional and highly variable in terms of the location and extent along an ice island’s perimeter. Recognizing the potential importance of the dimensions, Sazidy et al. (2019) approached the problem using 3D Finite Element Analysis (FEA) software. Smith (2020) built on the work of Sazidy et al. (2019) and recreated observed footloose-type calving events that were identified in the CI2D3 Database. Smith (2020) looked at the maximum principal stresses that resulted from failure of the observed geometries and a range of possible ice island thicknesses and ram lengths, since thickness and ram length were not known. The results of Smith (2020) are discussed in more detail in Section 5.3.

England et al. (2020) incorporated footloose calving into the analytical iceberg drift and deterioration model of Wagner et al. (2017). Rather than using a wave formulation to erode ice at the waterline and thereby create the rams that result in footloose failures, they approximated footloose calving of tabular icebergs as a stochastic process. In their analysis of ice island drift in the Geophysical Fluid Dynamics Laboratory global ocean model (GFDL OM4), Huth et al. (2022a) found that ice islands modeled as Lagrangian particles travel to unrealistic latitudes due to a lack of physically realistic fracture models. They incorporated footloose calving based on the England et al. (2020) parameterization, replacing the stochastic element with semi-empirical formulae for sidewall melt and wave notching. With the footloose mechanism represented, Huth et al. (2022a) found simulated ice island areas and trajectories closely matched observations. This suggests that the footloose mechanism (or similar edge-wasting process) is a major factor in ice island decay that was previously unaccounted for in climate models. In Huth et al.’s (2022a) parametrization, the underwater ram is assumed to form on all sides of the ice island and a fragment is calved randomly when the ram around the ice island perimeter exceeds an area that is defined by dimensions of the ram and the predicted footloose event. The length and width dimensions of the ice island are then adjusted by the same value to maintain its overall shape. There are several important differences between the work by England et al. (2020) and Huth et al. (2022a) and the analyses presented here. This includes the parameterization of thermal melt, and the way in which ice calved due to the footloose process is removed from the parent ice island. Most importantly, previous work has relied on broad statistical comparisons to illustrate the influence of the footloose mechanism while here we are able to make direct comparisons between model predictions and observed time series of the length and area of individual ice islands.

It should be noted that there is some potentially conflicting nomenclature for the lateral dimensions of rams and the icebergs that are produced by ram failure. Here, the distance from the wave notch to the outer face of a ram is the “ram length” (L_{ram}). The distance over an axis running perpendicular to the ice edge from the wave notch to the

point of maximum stress is x_{max}. The "failure width" (W_F) is defined as the straight-line distance over the calved region, roughly parallel to the ice edge (Fig. 2). We refer to the ice island from which the footloose mechanism removes surface area as the "parent" ice island. The calved piece, if intact and of sufficient size, is the "child" ice island. Parent and child ice islands are tracked in the CI2D3 Database if they are >0.25 km^2 in surface area.

This paper focuses solely on lateral deterioration and does not address surface or basal melt. Basal melt, in particular, can play an important role in ice island deterioration and the injection of fresh water into the upper ocean. However, in terms of the reduction in volume of a parent ice island, deterioration that impacts the lateral dimensions is most critical. For example, Wagner and Eisenman (2017) found that wave erosion was responsible for 70 % of mass loss in their modeling study of iceberg drift and meltwater distribution. Furthermore, Crawford et al. (2020) reported that the volume of "Petermann Ice Island-A-1-f", an ice island that was grounded in Baffin Bay, reduced by 67 % due to processes that caused a reduction in the lateral extent of the ice island. The ice island's volume was only reduced by 7 % over that two-year period as a result of melt of the horizontal surfaces.

3. Modeling ram growth and calving

Footloose calving results from buoyancy forces generated by an ice island ram, which is a result of waterline wave erosion. Full details of the underlying theory are in Appendix A. We bring forward the main equations and points of interest here.

Waterline wave erosion is calculated using the equations from White et al. (1980). The wave-induced melt rate (V_m in m s^{-1} °C) at a given depth (z) at a smooth wall is,

$$V_m(z) = \left(\frac{H}{\tau}\right) a Re_H(z)^{-0.12} \cdot \Delta T \tag{1}$$

where H is wave height, τ is wave period, a is an empirical constant (1.5×10^{-4} °C^{-1}) and ΔT is the difference between the far-field ocean temperature (T_∞) and the ice melting temperature T_m (Eq. A.2). Re_H(z) is the depth-dependent wave Reynolds number, which decreases with depth in the water column due to an exponential decrease in wave orbital height with depth (Eq. A.3). Melt is therefore greatest at the surface, which results in the formation of the characteristic wave notch.

An overhanging slab and an underwater ram will both grow with the development of a wave notch. The overhanging slab will calve close to the root of the notch and will produce relatively small ice fragments. The calving of overhanging slabs is further described in Section A.2 and the work of White et al. (1980). Mechanical failure due to the buoyancy forces imposed by the ram growth will typically occur at a location further towards the center of the ice island. Footloose-type failure will then dominate the lateral erosion of an ice island over time. We therefore focus on footloose-type failure in this modeling analysis as we look to assess the ability of models to predict the lateral erosion of an ice island over long time spans.

Footloose-type, buoyancy-induced failure will occur when the length of the ram (L_{ram}) reaches a critical length (L_{crit}),

$$L_{crit} = \gamma \sigma_F \left[\frac{h_T}{E}\right]^{1/4} \tag{2}$$

where σ_F is the failure stress (the stress at the base of the ice island at which fracture is assumed to occur), h_T is the ice island thickness, E is the effective Young's modulus and γ is a material parameter calculated from a set of variables that is assumed to be constant (Eq. A.7). We note that our σ_F is equivalent to the yield stress term used in previous studies (e.g., Wagner et al., 2014). Failure will then occur at the point of maximum stress (x_{max}),

$$x_{max} = \frac{\pi}{4\beta} \tag{3}$$

The parameter β has units of m^{-1} (Vaughan, 1995). It determines the wavelength of the bending of the ice (Eq. A.10). The maximum stress (σ_{max}) at x_{max} has magnitude

$$\sigma_{max} = \frac{E}{(1-\nu^2)} \frac{2P_1\beta^3 h_T}{\rho_w g} \cdot \exp[-\pi/4] \cdot sin[\pi/4] \tag{4}$$

(Watts, 2002), where ν is Poisson's ratio, ρ_w is the water density, g is acceleration due to gravity, and P_1 is the buoyancy force approximated as a point force acting at the ice front (Eq. A.12).

These solutions to the beam equations are based on the assumption that the ice material extends to infinity in the x-direction away from the free face. This assumption is valid for very large ice islands, but when the lateral extent of the ice island is relatively small, the free-floating ice island can tilt in response to the added upward force on one side (Smith, 2020). Fenz and Kokkinis (2012) investigated the effects of finite beam length in the x-direction (i.e., moving towards the center of an ice island along the axis perpendicular to the ice edge) on the resulting moments and stresses when ice floes contact a sloping structure. Using the equations of Fenz and Kokkinis (2012) with our base-case values in Table 1, we show that significant differences in the location of maximum stress and the stress magnitude begin to develop for ice islands when the dimension on which the forces are acting is less than approximately 1000 m (Fig. 3). There is a greater than 50 % reduction in the maximum stress when the ice island length is reduced to 500 m or less. In the following analyses we assume the ice island lengths and widths are large and therefore tilting is not of relevance. We then only simulate the deterioration of ice islands with lengths >1000 m in the evaluation of footloose calving using the ice islands in the CI2D3 Database (Section 5).

The footloose mechanism will result in more mass loss than if failure occurred at the notch root and the average lateral erosion rate erosion will be significantly larger than the rate of notch growth. Similar to the calving "amplifier" or "multiplier" described by Benn et al. (2017), O'Leary and Christoffersen (2013) and Slater et al. (2021) for calving from tidewater glaciers, we can calculate a multiplier (C^+) to link waterline wave erosion to footloose-type fracture:

$$C^+ = \frac{(x_{max} + L_{crit})}{L_{crit}}. \tag{5}$$

Fig. 4 shows the effect of ice thickness (h_T) on C^+ with the default parameters from our model. For example, for the base-case ice island that is 90 m thick (red dot, Fig. 4), the local rate of lateral erosion resulting from wave-induced waterline melt leading to footloose-type calving is about 16 times greater than the rate of wave-induced

Table 1
Default parameters assignments unless stated otherwise.

Parameter	Symbol	Value	Units
Ice island length	L	2000	m
Ice island total thickness	h_T	90	m
Ice island keel thickness	h_K	79	m
Ram length	L_{ram}	30	m
Effective Young's modulus	E	1	GPa
Failure stress	σ_F	200	kPa
Poisson's ratio	ν	0.33	–
Acceleration due to gravity	g	9.81	m s^{-2}
Wave height	H	2	m
Wave period	τ	7	s
Driving temperature	ΔT	5	°C
Thermal conductivity of sea water	k_w	0.563	W m^{-1} °C
Kinematic viscosity of sea water	ν_w	1.83×10^{-6}	m^2 s^{-1}
Latent heat of melting	Γ	333,000	J kg^{-1}
Sea water density	ρ_w	1024	kg m^{-3}
Ice density	ρ_i	900	kg m^{-3}
Differential ice/water velocity	u	0.2	m s^{-1}
Prandtl Number	Pr	13.1	–

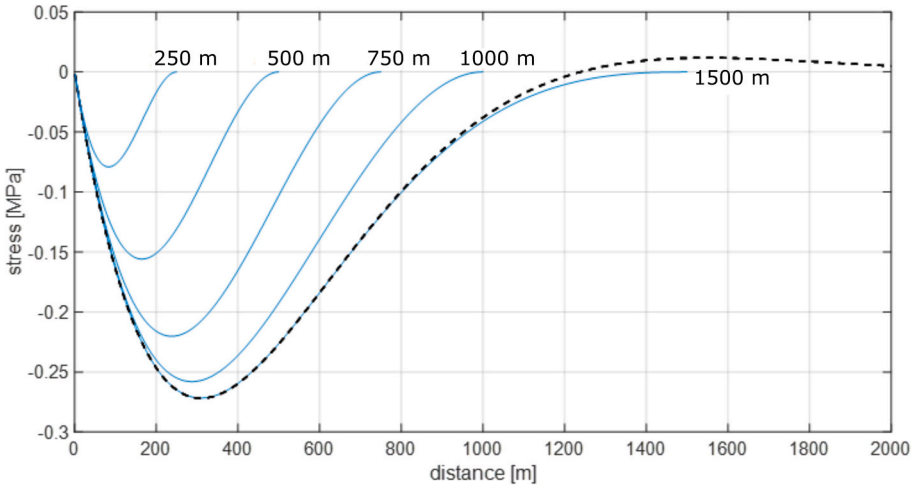

Fig. 3. Comparison of bending stress from semi-infinite beam calculations (dashed black line) and beams of finite lengths (blue lines) for an ice island with a 30 m long ram using parameter assignments from Table 1. The distance is measured from the root of the wave notch. (For interpretation of the references to color in this figure legend, the reader is referred to the web version of this article.)

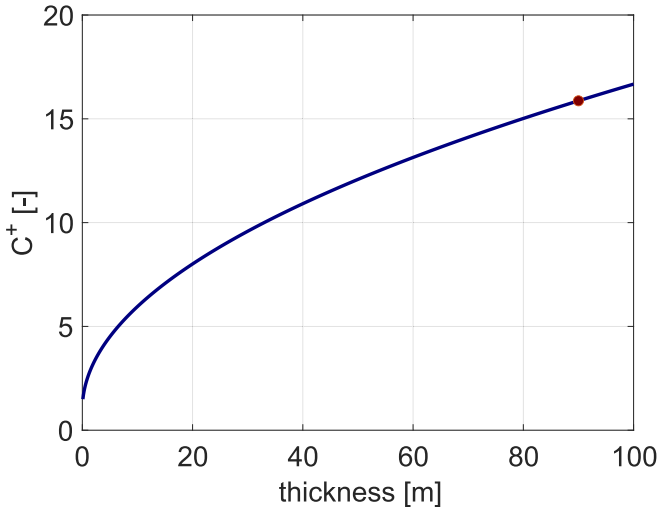

Fig. 4. Calving multiplier (C^+) as a function of ice island thickness. The red dot corresponds to the base-case ice-thickness value (90 m) assigned in this study.

waterline melt on its own. The value of C^+ is, by design, independent of the waterline notch growth rate, but increases with increasing E and h_T, and decreases with increasing σ_F.

It should be emphasized that the preceding calculations are based on 1D theory. Ice island fracture is inherently a 3-dimensional process, and in Section 5 we consider some of the effects of the higher dimensions on real world estimates of deterioration associated with waterline wave erosion and resulting calving processes. This is done using observations contained in the CI2D3 Database (section 4).

4. The CI2D3 Database

The CI2D3 Database is composed of over 25,000 records of ice islands during their drift following calving from four ice shelves and floating glacier tongues in northwest Greenland. Each record contains geospatial, morphological, and ancestral data of the ice island that was identified in satellite-borne synthetic aperture radar scenes. The ice islands were monitored until their surface area fell below 0.25 km^2. Database creators strove to include a record of a tracked ice island at least every two weeks. The data is reposited in the open-access Polar Data Catalogue (https://www.polardata.ca/pdcsearch/?doi_id=12678) (Desjardins et al., 2018) and is detailed in full in Crawford et al. (2018a).

In this study, we use records associated with Petermann ice islands (PIIs) that calved from the Petermann Glacier in 2008, 2010 and 2012. These make up the majority of records (68 %) within the CI2D3 Database. Each ice island record contains a georeferenced polygon geometry field of the ice island's surface extent. Surface area and length were derived from these manually-digitized polygons. For this study, the length of each ice island was calculated as the greatest distance between any two vertices of a polygon.

A unique aspect of the CI2D3 Database is the log of an ice island's ancestry, or "lineage". First, we use the lineage information to track the longer-term lateral erosion of parent ice islands and verify our models for simulating length and areal deterioration of ice islands (Sections 5.1 and 5.2). We then use the lineage to select parent and child ice islands associated with identified footloose mechanism calving events (Section 5.3).

5. Evaluation of the ice island deterioration model

For the analyses of longer-term erosion we excluded PII observations that were within substantial concentration of sea ice. Sea-ice concentration as mapped by the CIS in the agency's weekly, regional charts was extracted at the centroid of each ice island polygon. We retained PII observations within 1/10th sea-ice concentration or less. Future iterations of the model could include a sea-ice concentration variable as incorporated in the decay model by Huth et al. (2022a). Ice island "branches" were isolated using the lineage record in the CI2D3 Database and the igraph package (v1.2.2) for the R programming language by tracing successive observations of a tracked ice island. Branches initiate at the first observation of an ice island. If an ice island fractured into two or more children, the original branch would continue to track the largest of the children. New branches would track the child ice islands generated from that fracture event, and so on. An ice island branch was truncated if the ice island length fell below 1000 m. We excluded four branches because of digitization errors during the CI2D3 Database generation. We also removed one branch in which an obvious, non-footloose calving event split a large ice island in two within 10 h of the ice island being tracked. Fig. 5 shows the drift tracks of the ice island branches used in the modeling analysis and Fig. 6 shows the length and area distributions of the initial observations of each branch.

For each of the 121 ice island branches retained from the CI2D3 Database, the observed locations and times were linearly interpolated to produce time series of latitude and longitude at regular 24-hr intervals

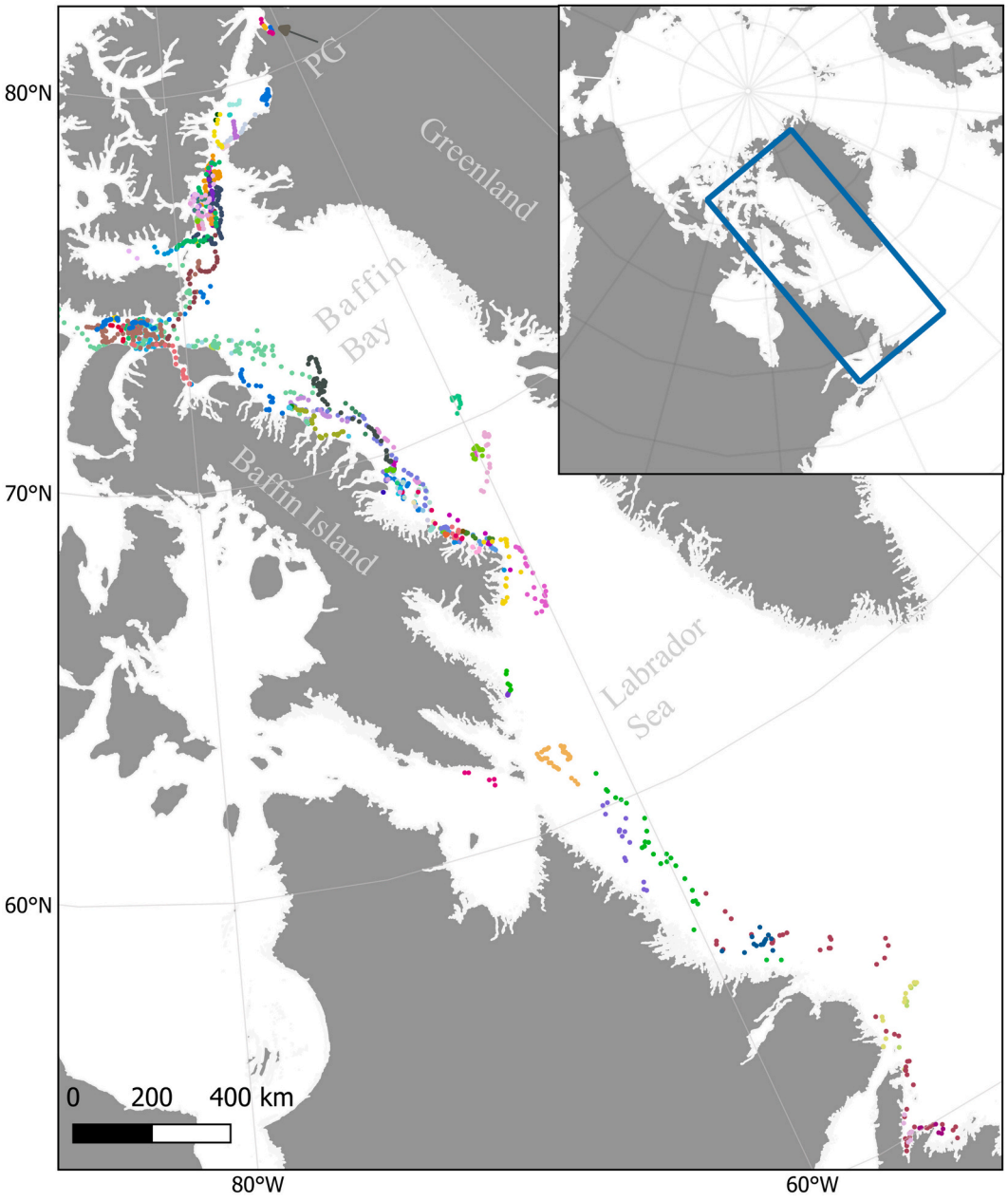

Fig. 5. Point locations of ice island observations as identified with satellite-borne synthetic aperture radar and recorded in the CI2D3 Database. Ice island branches used in the modeling analysis are differentiated by color.

matching the ERA5 environmental reanalysis product. Environmental variables included in the product are available at hourly intervals over a 30 km grid (C3S, 2017). The wave height (H), mean wave period (τ) and sea-surface temperature (SST) values for each point in the drift time series were determined from 2-dimensional linear interpolations of the values at the 4 ERA5 grid points enclosing the ice island position (Fig. 7). Wave-induced waterline melt was determined using Eq. 1, and forced-convection melt at the submerged face was calculated from Eq. A.4. Ram growth is then the difference between the rates of melt at the waterline and submerged face. We assign $h_T = 90$ m. This was held constant for all cases because the actual thicknesses of the ice island were not known. Limitations arising from this are discussed further below. A footloose fracture then occurred at $x_{\max} = 319$ m whenever L_{ram} reached the base-case value of $L_{crit} = 21.4$ m. These values for L_{crit} and x_{max} are derived from Eqs. 2 and 3 using values from Table 1. We note that this value of L_{crit} should be regarded as a lower bound, since we ignore the role of a downward bending movement at the ice edge due to vertical imbalances of the cryostatic and water pressures (Reeh, 1968). These have been found to increase L_{crit} by 15 to 50 % (Mosbeux et al., 2020).

The footloose calving model described in Section 3 and Appendix A was run for the time series of all branches selected above and the resulting time series of length (Section 5.1) and area (Section 5.2) were compared to the length and area of the CI2D3 Database record. A smaller subset of the CI2D3 Database was analyzed for a 3D stress analysis that assessed how the dimensions impact calving via the footloose mechanism (Section 5.3).

5.1. Simulating length change

Ice island length, the maximum waterline dimension, is used as the measure of iceberg size in operational models such as the NAIS model

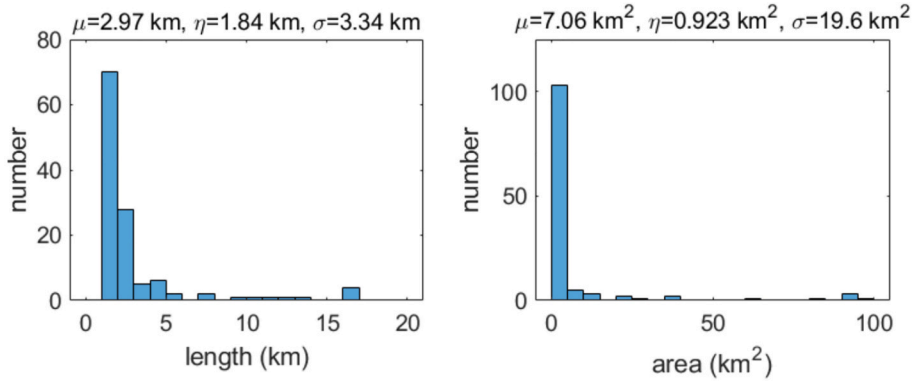

Fig. 6. Length (left) and area (right) distributions for the first observation of all ice island branches used in the modeling analysis. The mean (μ), median (η) and standard deviation (σ) are provided for each distribution.

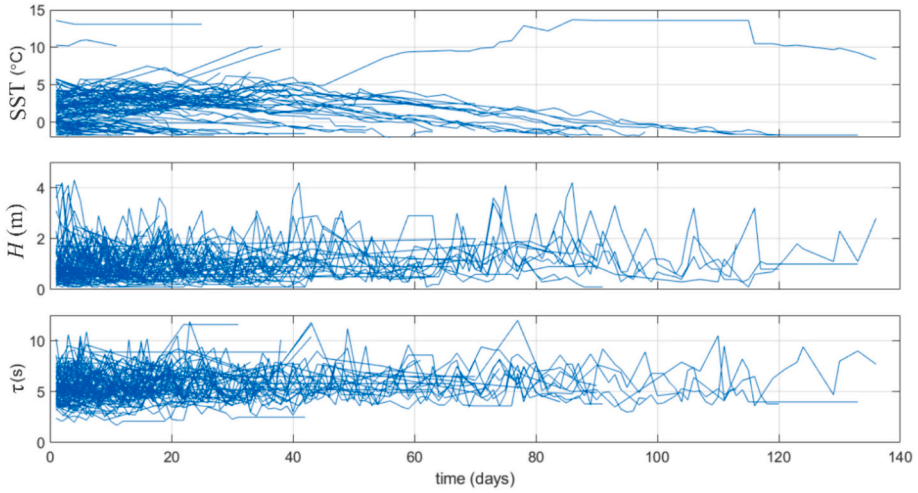

Fig. 7. Timeseries of environmental variables applied at each timestep of each ice island simulation. The variables used to drive the model were sea-surface temperature (SST; top), wave height (H; middle) and mean wave period (τ; bottom).

used at the CIS (Kubat et al., 2007; Motz, 2022). It is therefore a fundamental dimensional variable to evaluate. In the following analyses we compare observed changes in ice island length to modeled length changes. The modeled length change is taken to be the cumulative length reduction predicted by the wave notch and footloose calving model, assuming that all calving occurs along the length dimension, and ice island width (perpendicular to length) is unaffected. This will clearly not be true in all cases, particularly as an ice island can rotate during

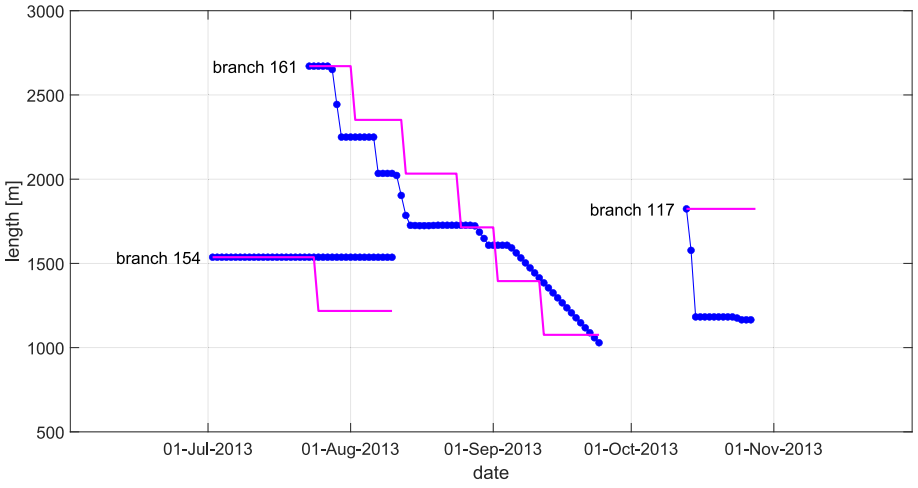

Fig. 8. Examples of footloose model (blue) vs observed (pink) length change for three individual ice island branches. Branches were numbered before filtering to the final set of records used in the modeling analysis. (For interpretation of the references to color in this figure legend, the reader is referred to the web version of this article.)

drift. However, this implementation provides a starting point for the model evaluation. We also compare the observed length reductions to the results of a zero-melt model, in which the initial observed length is held constant, and a thermal-melt model, in which the rate of length reduction equals the rate of wave notch growth on one side of the ice island.

For 41 of the ice island branches, the sea-surface conditions were not conducive to calving, so both the observed and modeled time series showed that no calving took place. In these cases the model error was at or near zero. Fig. 8 shows selected examples of cases where calving was observed. Branch 154 shows a scenario in which the ice island was observed to change length through one calving event, but the modeled wave notch growth over the simulated period was insufficient to result in fracture. Branch 117 displays the opposite scenario. Here, there was no observed change in length, but the footloose model predicted multiple calving events. Branch 161 is an example in which the footloose model performed very well. Numerous length changes were observed and are captured by the footloose model. After 74 days and a length change of about 2000 m, the predicted and observed lengths are almost identical.

The value of the CI2D3 Database is that it contains a sufficient number of tracked ice island observations to move beyond individual cases and examine model performance statistics. We examined if model error corresponded with SST, ice island length or latitude, and the year in which the ice island calved from the Petermann Glacier. The year of calving was considered because the ice island thickness would affect L_{crit} and x_{max} and the rate of length reduction, and the ice islands that calved from Petermann Glacier in 2008, 2010 and 2012 had differing mean thicknesses (Crawford et al., 2018b; Crawford and Mueller, 2023). However, we did not find any meaningful relationship between model error and any of these variables (SST, length, latitude or year of calving).

In regards to thickness, the assessment of model error and thickness is challenged given the limited spatial coverage from which the average thicknesses of the original Petermann ice islands were previously derived (Crawford et al., 2018b), the spatial variability in those thicknesses, and the non-uniform thinning of individual ice islands over time. This makes it difficult to estimate the thickness of a particular ice island at the time of its observation. We note that $L_{crit} \sim h_I^{1/4}$ and is therefore only weakly dependent on ice thickness. However, $x_{max} \sim h_I^{3/4}$, which is more strongly varying with thickness.

Fig. 9 shows the time series of the model error (observed minus modeled ice island length), color coded by the observed ice island length. Points that lie above the zero line correspond to cases in which the model over-predicts length reduction, so the modeled length is shorter than the observed length. Correspondingly, points that lie below the zero line correspond to cases in which the model under-predicts length reduction. The increasing spread in model error with elapsed time is shown with the root mean squared error (RMSE) (red line in Fig. 9).

The solid black line in Fig. 9 shows the mean model error on each day. Before day 20 there is a very small under-prediction on average. There are 69 ice island simulations that run to at least 20 days of elapsed time, and many of the simulations have close to zero error over this period. The model starts to over-predict length loss soon after this and the mean model error hovers around 300 m between 40 and 80 days of elapsed run time. Over this time period the mean daily error across all simulations has a maximum of 367 m, a minimum of 199 m and a mean of 274 m. The model starts to under-predict length again on day 84 and the mean error value drops substantially and becomes negative. We note that the results after these many elapsed days are impacted by a decreasing sample size.

We find that the footloose model performs well out to 80 d of elapsed run time, at which point the mean model error is +277 m. This is a large improvement compared to the mean model error at 80 d for the zero-melt model (−1545 m) and the thermal-melt model (−1403 m). The mean error from the footloose model over 10 to 80 d is +170 m. This average value can be reduced to near zero by decreasing the footloose deterioration rate by 8 %. However, we have not re-run the model with different parameters in order to achieve this, as there are many small changes or combinations of changes that could give the desired reduction.

There are many possible reasons why the footloose parametrization over-estimates the length reduction of the ice island branches tracked in the CI2D3 Database. First, we always apply the loss from a footloose calving to the length dimension. In reality, footloose calving could occur at a location on the ice island perimeter where it would not impact the ice island length. The over-estimation could also result from the White et al. (1980) parameterization of wave notch erosion, which is based on scant laboratory evaluations, or from an overestimation of the distance between the wave notch and fracture location (x_{max}) due to uncertainty in the non-uniform thickness of the ice islands, and the neglect of the frontal pressure imbalance discussed above. We also do not account for potential deceleration of wave-induced waterline erosion as the ram grows. In addition, some deterioration may have been overlooked due to the resolution of the satellite imagery and the digitization process used in the generation of the CI2D3 Database. Uncertainty also exists in the ERA5 environmental data, our interpolation scheme, and our assignment of σ_F and E. Weakening through pre-existing cracks and crevasses is also not considered. This could lead to both over or under-prediction of wave notch growth and footloose failure. Investigations into how pre-

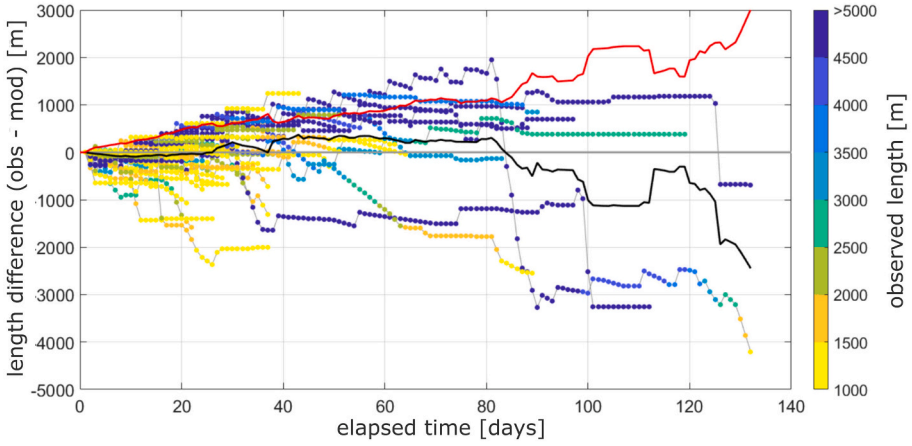

Fig. 9. Time series of model error in length (i.e., CI2D3 Database observed ice island lengths minus footloose-modeled lengths), color-coded by ice island length. The black and red lines show the mean model error and RMSE, respectively. (For interpretation of the references to color in this figure legend, the reader is referred to the web version of this article.)

existing weaknesses influence the timing and magnitude of calving, including through the footloose mechanism, are out of the scope of our study. However, this is an important area for future research. Underprediction is largely the result of other fracture mechanisms influencing the deterioration of (large) ice islands, as discussed above. However, despite the numerous sources of model uncertainty, the footloose model shows strong performance and is a notable improvement in comparison to other ice island deterioration models that do not consider the footloose mechanism.

5.2. Simulating areal change

In some research applications (e.g., climate impacts of ice island melt-water) it is important to know the change in ice island area (e.g., Crawford et al., 2018b; Merino et al., 2016). Huth et al. (2022a) apply an approach to simulating ice island areal change in which the growth of the ram length is assumed to occur on all sides of an ice island and calving events seem to be nearly continuous. Similarly to Huth et al. (2022a), we assume a rectangular ice island with a constant length to

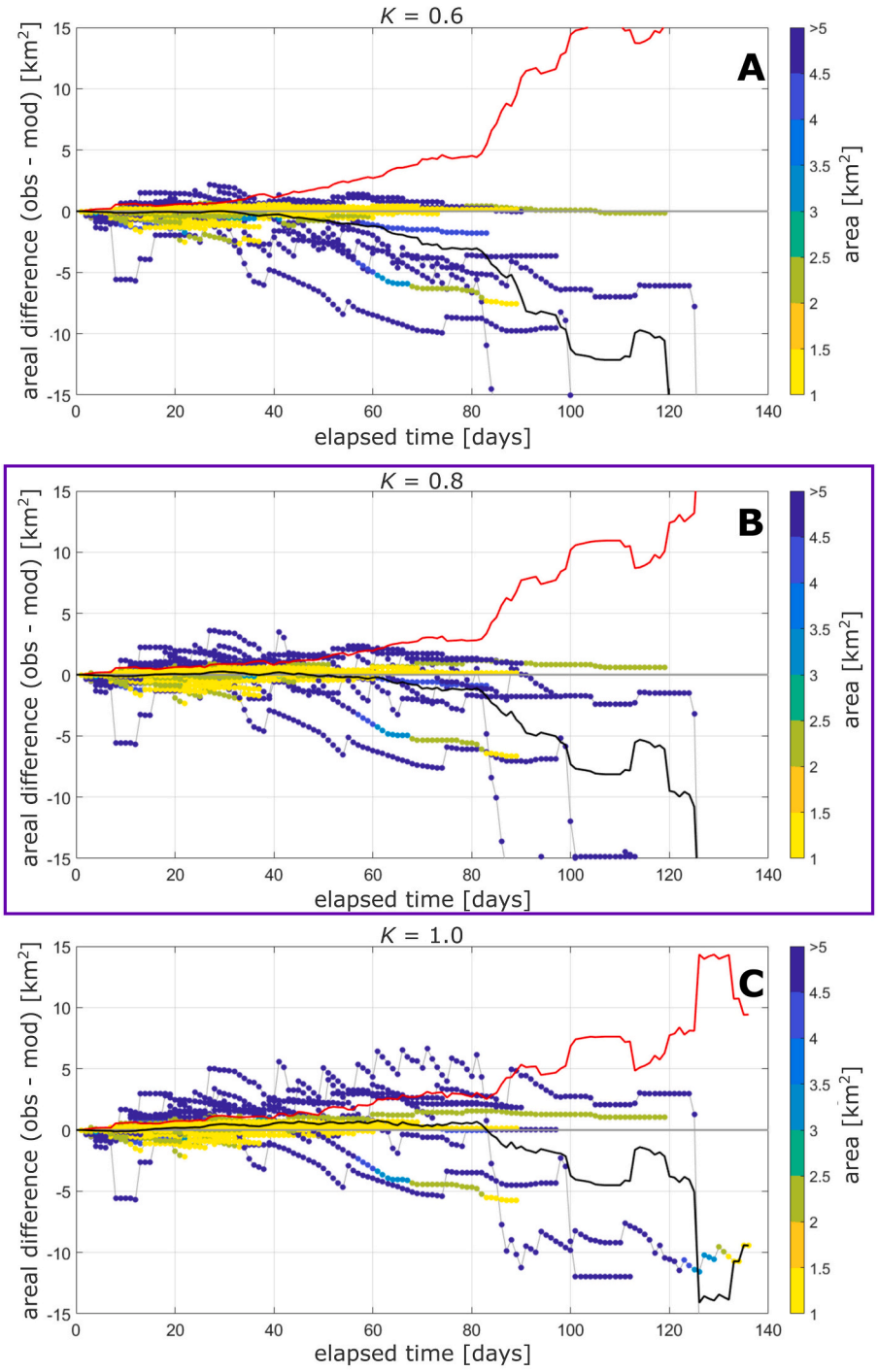

Fig. 10. Time series of model error in area (i.e., CI2D3 Database observed ice island area minus footloose-modeled area), color-coded by observed ice island area. The black and red lines show the mean model error and RMSE, respectively. The three plots show model error with varying values assigned to the coefficient (K) that determines the width of a footloose calving event relative to the ice island length: A) $K = 0.6$, B) $K = 0.8$, C) $K = 1.0$. The model best fits the observations with $K = 0.8$. (For interpretation of the references to color in this figure legend, the reader is referred to the web version of this article.)

width (*L*:*W*) ratio (*r*) in our approach to simulating areal change. However, we model discrete calving events and assume that wave action occurs along one side of an ice island's length axis. We first solve for the length dimension of the calving event using the equations presented in Section 3. We then take the width of the footloose event (i.e., the dimension parallel to the ice edge; W_F) to be $K \times L$. We tune the coefficient *K* by matching the areal change simulated by the footloose model with the observations in the CI2D3 Database.

When a footloose calving event occurs, the area of the ice island is reduced by $K \times L \times x_{max.}$ The *L*:*W* ratio is preserved between two timesteps (t, $t+1$) of the model through adjusting the *L* and *W* dimensions with:

$$L(t+1) = \sqrt{A(t+1) \times r}\,, \tag{6}$$

$$W(t+1) = \sqrt{A(t+1) \times 1/r} \tag{7}$$

where *A* is the ice island surface area. Here, we set $r = 1.6$, as previously assigned by Crocker (2012). Using GIS we measured the approximate *L* and *W* of the ice islands considered by Smith (2020), with the width being measured across the widest distance falling perpendicular to the length axis. The mean *r* of these ice islands ($n = 26$) was 1.8. This value decreased to 1.7 when we removed repeat observations of an ice island that sustained multiple footloose events. We note that our results are not substantially impacted when *r* is adjusted between 1.6 and 1.8.

Fig. 10 shows model error in areal change with elapsed simulation time. As above, positive values correspond to cases in which the model over-predicts area reduction. The points in Fig. 10 are colored by observed ice island area, showing that the larger model errors are associated with ice islands that have greater surface areas. The larger size of these ice islands simply makes it possible for greater model error to exist.

The three panels of Fig. 10 show the impact of altering *K* from 0.6 to 0.8 to 1.0, with the solid black lines again showing the mean model error on each day. When *K* is assigned a value of 0.8, the mean model error is near 0 until approximately 60 days of simulation (Fig. 10B), which is the best model fit as shown in Fig. 10. A histogram of model error at day 20 shows a central tendency at this point in the area simulations (Fig. 11). The majority of the model error values are 500 m or less at this time.

The model has a negative bias as time elapses past day 70 (Fig. 10). Mean model error remains relatively small (~1 km^2) until 80 days of simulation, after which there are several instances in which the model greatly underestimates observed areal change. Model error increases rapidly, with the RMSE greatly increasing at this point. Again, this is impacted by the small number ice islands branches that remained intact for these longer durations.

Underestimates in the decrease of ice island area may result from our modeling approach that always initializes the model without a wave notch, when a wave notch could have been eroding the sidewalls of the observed ice islands before the start of our simulations. This would result in a footloose calving event to occur earlier than our modeling would predict.

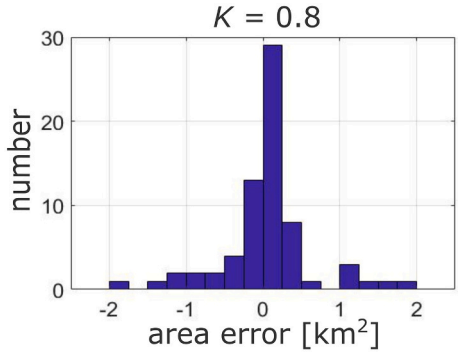

Fig. 11. Histogram of model error of area (i.e., CI2D3 Database observed ice island area minus footloose-modeled area) at 20 d of elapsed simulation time.

Ice islands can rotate during drift, which will impact the rate of wave notching and footloose-type calving around their perimeters. In simulating length change, our assumption that footloose calving acts only on the length dimension may therefore be close to an upper bound. However, when simulating areal change, we modify the length and width dimensions of the ice island through the inclusion of the coefficient *K*. While this is performed in a highly idealized way, our validation efforts demonstrate that the model performs well. The approach also implicitly captures deterioration occurring to all sides of the ice island through the L:W scaling parameter, *r*.

We consider all areal deterioration of the modeled ice islands to have occurred through footloose failure. The model does not account for other large-scale fracture mechanisms that could have rapidly and sporadically reduced the areal extent of some ice islands. Such large-scale fracture could be influenced by grounding on bathymetric high points. The CI2D3 Database contains records of ice islands drifting or grounded status, showing that one of the 121 ice island branches included in our study was grounded over its full duration. Twenty other branches had instances of grounding over the periods that they were tracked. While we do not account for large-scale fracture mechanisms or consider the grounded status of an ice island, the model performs very well over about 2.5 months of simulation time when the coefficient *K* is set to 0.8. This duration is much longer than necessary for tactical forecasting. Those using the model in other applications (e.g., climatological research) will want to test the sensitivity of their results to varying *K*.

5.3. 3D analysis

The footloose fracture analysis presented by Wagner et al. (2014) considers an idealized 1D beam. It is not clear, a priori, how representative the formulae presented in Section 3 are for 3-dimensional ice islands which have irregular shapes. To assess footloose failure in 3D, Sazidy et al. (2019) used commercial 3D FEA software (LS-Dyna ®) to generate meshes and an element erosion technique to analyze stresses and fracture of ice islands that were observed to experience footloose-type failures. Smith (2020) used the model of Sazidy et al. (2019) to recreate observed footloose type calving events from ice islands contained in the CI2D3 Database (Crawford et al., 2018a). The FEA modeling of footloose calving conducted by Smith (2020) provides a basis for investigating how the 3rd (lateral) dimension of an ice island affects the characteristics of footloose calving, and how the 3D case might differ from the analysis of Wagner et al. (2014) and that presented in Section 3.

Smith (2020) mined the CI2D3 Database for instances of footloose calving that resulted in child ice islands that were large enough to be subsequently tracked in the CI2D3 Database, and performed FEA modeling of 3D meshes representing each ice island immediately prior to the footloose calving event. Following a series of identification and sub-setting steps described in Smith (2020) there were 26 ice islands in the subset of potential footloose calving events, the lengths of which were measured in QGIS for this study. Smith (2020) generated 3D meshes for each of the 26 parent ice islands with prescribed rams that were simulated at the observed calving edge of the ice island. Individual meshes were created for each ice island with L_{ram} of 20, 40 and 60 m. When extruded, the total thickness (h_T) and thickness of the ram (or keel, h_K) were 80 and 70 m, respectively. The extruded meshes were used to initialize a simulation in LS-Dyna ® using LS-Solver. Of the various outputs considered by Smith (2020), we are most concerned here with the maximum of the Maximum Principal Stresses (MPS), which is the greatest stress across all elements through time in an FEA model simulation. We removed five outlier MPS values based on Cook's Distance (Neter et al., 1996). These values were also removed in the

analysis presented by Smith (2020).

Fig. 12 shows the relationship between L_{ram} and the maximum MPS from the FEA analysis of the selected footloose cases identified from the CI2D3 Database. The theory detailed in Section 3 suggests that maximum stress should be linearly related to ram length and the 3D FEA analyses show a similar effect (on average), although there is considerable scatter.

The FEA modeling analysis shows that the maximum stress varies significantly for any given real 3D shape with an assumed ram length. As seen in the histograms included in Fig. 13, the distribution of the maximum MPS is highly skewed for small ram lengths (e.g., $L_{ram} = 20$ m in this assessment). For larger values of L_{ram} the distribution becomes more uniform, although the coefficient of variation (the standard deviation divided by the mean) stays between 0.20 and 0.34 for the three ram lengths that were tested.

The FEA can also be used to compare the 1D and 3D stress magnitudes (Fig. 13). To make a valid comparison we first note that Smith (2020) used different parameter values than the base-case values in the present study. In particular, their assigned value of E was larger (9 GPa). We also note that the maximum 3D FEA MPS reported by Smith (2020) are not exactly equivalent to the 1D maximum tensile stresses (σ_{max}) from the beam equations. However, the maximum FEA MPS are tensile, a reasonable distance from the ice edge, and approximately in the vertical plane, which suggests that a comparison is meaningful as long as the analyses are performed with the same ice properties.

When the 1D calculations, presented in Section 3, are solved with the values used by Smith (2020) for E and h_T, the mean maximum stresses from the FEA (maximum MPS) are approximately 25 % greater than σ_{max} (Fig. 13). The discrepancy may result from irregularities in the 3D shape impacting on stress magnitude and distribution, and potentially leading to stress concentrations. However, given the uncertainty in the numerous parameters that must be set in both the 1D and 3D simulations (e.g., E, h_T, mesh resolution), the comparison indicates that the 1D analytical equations provide a reasonable estimate of stresses in realistic 3D shapes.

The mean length (x_{max}) of footloose calving events identified by Smith (2020) was 416 m. Using Eqs. A.9 to A.11 and keeping the base values listed in Table 1, we are able to obtain a similar value (420 m) by adjusting E to 3.0 GPa or h_T to 130 m. These are the same parameters that are adjusted by Mosbeux et al. (2020) to accommodate cracked or crevassed ice. Our adjustments show that the model is able to reproduce values from the 3D FEA with tuned values that lie within reasonable bounds of the respective parameters. This indicates that our value assignments in Sections 5.1 and 5.2 were reasonable, and more broadly, shows that the 1D modeling approach described by Wagner et al. (2014) is able to reasonably determine maximum stress for observed "real world" ice islands.

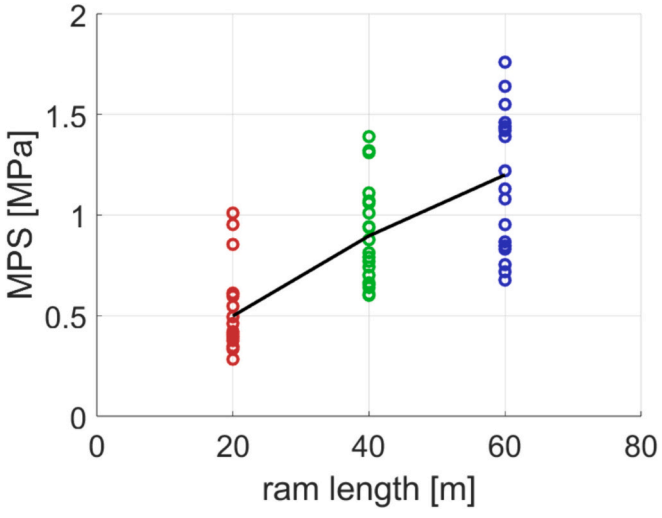

Fig. 12. Relationships between ram length and the maximum of maximum principal stress (MPS) determined by FEA for selected cases of footloose calving identified from the CI2D3 Database and presented by Smith (2020). Ram lengths used were 20 m (red), 40 m (green) and 60 m (blue). The ice island thickness was estimated at 80 m. The black line connections the mean values of the maximum MPS for each ram length. (For interpretation of the references to color in this figure legend, the reader is referred to the web version of this article.)

6. Discussion and conclusions

The analyses presented in this paper support the idea that the rate of wave-notch growth at the waterline, which leads to calving via the footloose mechanism, is a major influence on the lateral deterioration of ice islands. The footloose calving mechanism has previously been modeled or included in a number of studies (e.g., England et al., 2020; Huth et al., 2022a; Trevers et al., 2017; Wagner et al., 2014), and can be simulated using three oceanic variables: wave height, wave period, and sea-surface temperature. Given uncertainties in parameter assignments and the impact of irregular edge shape on stress distributions, our stress comparison shows that the 1D elastic model presented by Wagner et al. (2014) does a reasonable job of estimating stresses for realistic, 3D ice island geometries. Though this model assumes purely elastic behavior and ignores viscoelastic contributions, our analysis provides a foundation of support for the use of the approach to simulate footloose-style calving in models intended for operational or research purposes. For an in-depth discussion of the different roles that viscous and elastic deformations may play in footloose-type calving, see Mosbeux et al. (2020).

Using observational records of ice island length and area contained within the CI2D3 Database to directly assess the model's performance, we show that the 1D footloose model is able to reasonably predict ice island length for 80 days given the absolute model error remaining below 400 m across a large range of ice island sizes. The inclusion of the footloose mechanism in modeling of ice island deterioration shows substantial improvement in performance compared to models that do not include the fracture mechanism.

The CI2D3 Database allowed for the first large-scale assessment of the footloose model's performance in capturing change in ice island length. The database also provided an opportunity to assess our new approach to modeling areal change resulting from footloose calving. Our approach utilizes two parameters, K and r, which respectively determine the width of a footloose calving event and the length to width ratio, of the full ice island, that is maintained while an ice island deteriorates. With $K = 0.8$ and $r = 1.6$, the model simulated areal change of the tracked ice islands very well for 80 d, with the absolute mean model error staying below 1 km^2.

Our approach to modeling areal deterioration simulates discrete calving events and modifies the ice island length and width dimensions to maintain a constant length to width ratio. This differs from the approach proposed by Huth et al. (2022a), who also maintain a constant length to width ratio but consider footloose-style calving to occur in a more constant manner given ram growth around the entire perimeter of an ice island. Another noteworthy difference between the modeling work presented here and by Huth et al. (2022a) is the value assigned to the effective Young's modulus, E. Huth et al. (2022a) assign much lower values (0.01 to 0.1 GPa) than utilized in this study. These low values may have been necessary given the large relative thickness values (considering the small areal dimensions) of the Northern Hemisphere ice island size distribution used to initialize their model tests. As noted by Huth et al. (2022a), the size distribution provided by Bigg et al. (1997) skewed to the very small. Many ice islands easily reached the threshold dimensions under which footloose calving was turned off by Huth et al. (2022a); those that had surface areas greater than the cut-off threshold still had larger relative thicknesses compared to the ice islands

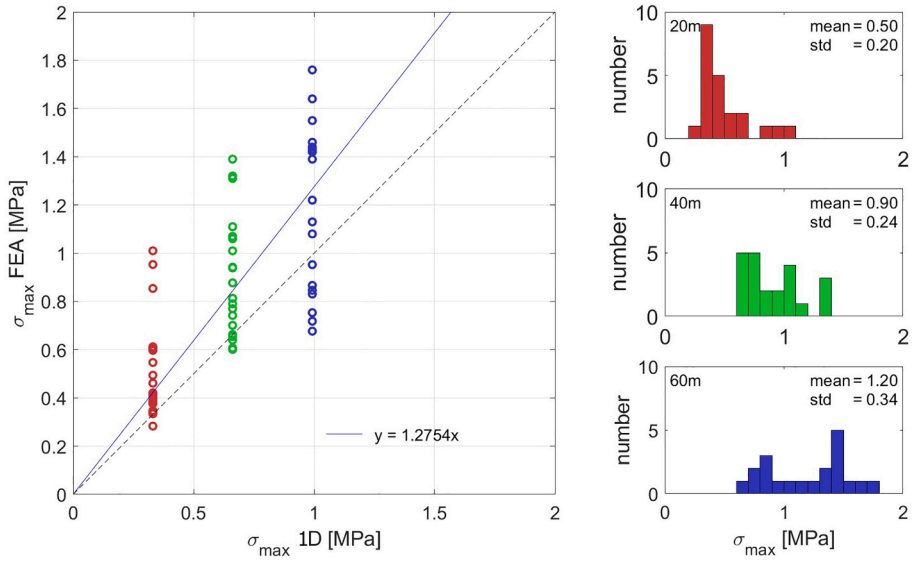

Fig. 13. Comparison of σ_{max} for modeled 1D footloose calving and the MPS from the 3D FEA of Smith (2020) for three ram lengths: 20 (red), 40 (green) and 60 m (blue). The value for E and h_T utilized by Smith (2020) in the 3D FEA were also assigned to the 1D footloose calving model in this comparison. The dotted line shows a 1:1 relationship. The solid line is the linear fit. (For interpretation of the references to color in this figure legend, the reader is referred to the web version of this article.)

associated with our CI2D3 Database records.

Iceberg models that have been applied for operational purposes have, largely, modeled length change. While we show the ability for the footloose model to simulate the length change of the waterline dimension of ice islands tracked in the CI2D3 Database, we note that long-term length simulations may not be necessary for operational purposes when there is access to frequent satellite imagery from which ice island dimensions can be updated. However, accurate short-term forecasts remain important for those modeling ice island trajectories for risk mitigation purposes.

Through our work presented in Section 5.2, we contribute a calibrated approach to incorporate the footloose model in models of ice island *areal* deterioration. These models are often utilized in research focused on the impact of ice island drift and deterioration on aspects of the larger-scale climate, which by necessity assign hypothetical ice island size distributions and individual ice island dimensions. We are interested in future modeling studies that implement our approaches to simulating the footloose mechanism for length or area change, and we see value in a study that compares output from climate simulations (e.g., meltwater distribution) when different iceberg decay approaches are applied. We also note that, to continue improving ice island deterioration models, the community should constrain the equations pertaining to sidewall melt presented by White et al. (1980) and further develop a method for modeling large-scale ice island fracture (see, e.g., Huth et al., 2022b) alongside the smaller-scale footloose-type calving.

Funding sources

AJC was supported by the Leverhulme Trust as an Early Career Fellow (ECF-2021-440). TJWW acknowledges NSF OPP grant #2148544.

Author statement

This is original work that has not been previously published. The work is not submitted for publication elsewhere and will not be if accepted for publication in *Cold Regions Science and Technology*. All authors have approved of the submitted manuscript.

CRediT authorship contribution statement

Anna J. Crawford: Writing – review & editing, Writing – original draft, Visualization, Project administration, Investigation, Formal analysis. **Greg Crocker:** Writing – review & editing, Writing – original draft, Visualization, Formal analysis, Conceptualization. **Jesse Smith:** Writing – review & editing, Formal analysis. **Derek Mueller:** Writing – review & editing, Project administration. **Till J.W. Wagner:** Writing – review & editing.

Declaration of competing interest

The authors do not have any competing interests to disclose.

Data availability

The Canadian Ice Island Drift, Deterioration and Detection (CI2D3) Database ver. 1.1 is available via the Polar Data Catalogue (DOI: 10.21963/12678). ERA5 data are available through the Copernicus Climate Change Service (C3S, 2017).

Acknowledgements

We appreciate the input provided by Richard McKenna in regards to moments and stresses resulting from the growth of ice island rams. We also thank all of the individuals and funders who supported the development of the Canadian Ice Island Drift, Deterioration and Detection (CI2D3) Database. The CI2D3 Database project was funded and supported by Environment and Climate Change Canada (ECCC), Polar Knowledge Canada, the Canada Foundation for Innovation, the Ontario Research Fund, and the Canadian Ice Service (ECCC). We also greatly thank the four anonymous reviewers who considered this work ahead of publication.

Appendix A. Ram growth and calving in 2-D

A.1. Waterline Melt

We determine waterline wave erosion using the theoretically-derived equations from White et al. (1980). The wave-induced melt rate at a given depth (z) ($V_m(z)$ in m s^{-1} °C) at a smooth wall is,

$$V_m(z) = \left(\frac{H}{\tau}\right) 0.00015 Re_H(z)^{-0.12} \cdot \Delta T \tag{A.1}$$

where H is wave height, τ is wave period, ΔT is the difference between the far field ocean temperature (T_∞) and the ice melting temperature T_m. Following Joseberg (1977), Løset (1993), and Kubat et al. (2007), the ice melting temperature is calculated from,

$$T_m = T_f exp\left(-\alpha\left(T_\infty - T_f\right)\right) \tag{A.2}$$

Where $\alpha = 0.19\ °C^{-1}$ and T_f is the seawater freezing temperature, which is set to −1.80 °C. This modification to the melting temperature is required given the complex melting and mixing processes at and adjacent to the ice surface (Kubat et al., 2007). Sea-surface temperature (SST) is assigned to T_∞ for the calculation of wave-notch growth. This assignment is necessary given the limited available data for this study and other operational or research-focused modeling of iceberg deterioration. We also note that temperature profiles can vary around an ice island (Morrison and Goldberg, 2012; Stern et al., 2015), so Eq. A.2 can be considered an approximation that accounts for several poorly constrained processes. With the default parameters given in Table 1, the use of Eq. A.2 results in waterline melt rates that are approximately 10 % higher than with a fixed value of $T_m = 0$ °C, and 20 % lower than with a fixed value of $T_m = -1.8$ °C. The effect of varying T_m on waterline melt is small when far field water temperatures are high but becomes more significant in cold water.

A variation in wave melt rate with water depth arises because the wave orbital height decreases exponentially with depth in the water column. The effective melt rate at z is calculated using Eq. A.1 and the depth-dependent wave Reynolds Number, $Re_H(z)$,

$$Re_H(z) = \frac{H^2}{\tau \nu_w} e^{-2kz}, \tag{A.3}$$

which depends on H, τ, and the water viscosity (ν_w). k is the wave number.

White et al. (1980) found that melt rates increased with surface roughness. The estimated melt rates are approximately 50 % higher for a surface with roughness elements with dimensions of 0.1 cm than for a case with a smooth surface. We use the smooth surface model because our observations indicate that although iceberg walls at depth can be grooved and cusped, the ice surface inside the wave notches tends to be smooth.

Of potential significance is the fact that the wave erosion equations of White et al. (1980) are related to the orbital velocities of waves in deep water. They do not account for the transition to shallow water above the ram, which modifies the wave properties. The few existing measurements of large rams (e.g., Diemand, 1987; Hodgson et al., 1988) suggest that at least sometimes the water depth over the ram is fairly constant. This is supported by many available aerial images of icebergs and observations by the authors in which the color of the water above the ram is broadly constant over the entire length of that ram (Fig. 1B). Since water color is affected by optical path length, if the water was significantly deeper at the outer edge of the ram it would appear darker. It seems likely that the motion of water particles in the region above large rams is affected by the relatively shallow depth and the effects of shoaling and in some cases, wave breaking. In order for the waves to continue to melt the waterline notch, the heat used for melting must be efficiently replenished. This could be through oscillatory exchange of water out over the front of the ram, or lateral movement of water along the face that is similar to longshore drift. If the heat is not replenished, the local water temperature will drop, slowing the ocean-to-ice heat transfer and rate of notch growth. The thermodynamic model suggests heat transfer depends linearly on temperature, so notch growth could be slowed significantly.

Kobayashi (1985) investigated the similar problem of wave erosion of permafrost cliffs, developing an analytical model that showed good agreement, qualitatively, to observed notching. We will not repeat his theoretical formulations here, but note that he suggests that the rate of notch growth is inversely proportional to the notch incision depth, which is equivalent to the ram length in our application. That is, as the notch deepens, the diffusion of heat to the notch face becomes less efficient (Barnhart et al., 2014; Kobayashi, 1985). In the analyses presented here we will assume that the notch growth equations of White et al. (1980) are roughly appropriate for all notch sizes, but note that this should be a topic for further investigation.

A.2. Overhang Calving and Ram Growth

As waterline melt progresses and a wave-notch grows, a slab of ice is produced in the sail over-hanging the wave notch (Fig. 2A). White et al. (1980) used FEA with an elastic rheology to assess the stresses in the ice that result from different notch and over-hang configurations. From the FEA they generated analytical expressions for the failure conditions based on notch fillet radius, over-hang thickness, and an assumed failure stress of 2.2 MPa. They then combined the failure criterion with the rate at which the wave notch forms (Eq. A.1, $z = 0$) to estimate the calving rate and the rate of mass loss due to calving.

Over long periods of time, *all* of the ice above the notch will be removed and the average rate of loss will be dependent solely on the rate of notch growth (V_m). Furthermore, if the growth of the ram also leads to mechanical failure, then the rate of notch growth would be the process controlling almost all mechanical deterioration at the ice island perimeter. The following discussion considers this process for a highly idealized geometry.

A.3. Ram Growth

Ram growth is the difference between the waterline notch growth (V_m) and the rate at which thermal processes act to erode the ram at its outer face (V_{rf}). Processes contributing to V_{rf} include the aforementioned wave erosion, forced convection, and free (buoyant) convection. Since melt at the ram face is typically much smaller than melt at the waterline, its effects are small and we use a relatively simple parameterization from Weeks and Campbell (1973) based solely on forced convection for its simulation. Weeks and Campbell (1973) derived an expression for forced convection melt of

large icebergs based on flat plate theory in which the average melt rate (V_{rf}) in m s^{-1} is,

$$V_{rf} = c \cdot u^{0.8} \cdot \Delta T / L_f^{0.2} \tag{A.4}$$

where c is the bulk heat transfer coefficient (6.74×10^{-6} $m^{0.4}$ $s^{-0.2}$ $^{\circ}C^{-1}$), u is the differential speed between ice and water and L_f is the length across the concerned ice face. Using the default values from Table 1, Eq. A.4 gives a melt rate of 0.26 m d^{-1}.

Bruneau et al. (2011) suggested that the temperature variation with depth is an important consideration in iceberg deterioration modeling. On the East Coast of Canada, spring and summer heating is often limited to a relatively thin surface layer (Crocker, 2001). Fig. A.1 shows AXBT (Airborne Expendable Bathy Thermograph) profiles collected off the northeast coast of Newfoundland in June 2001 (Crocker, 2003). The data show that, in this area, the warm upper layer was limited to approximately 15 m. At greater depth down the face to the ram the water remains cold, and thermal erosion of an ice island sidewall would be quite limited.

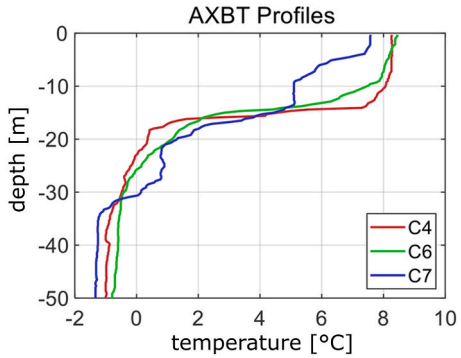

Fig. A.1. Water temperature profiles taken in the vicinity of icebergs from Crocker (2001) on June 21 (C4: 50° 00′ N, 55° 50′ W), June 22 (C6: 50° 19′ N, 53° 37′ W), and June 23, 2001 (C7: 51° 16′ N, 54° 56′ W).

Since we use the surface water temperature in the calculation of ΔT, our estimates of V_{rf} in Eq. A.5 are probably upper bounds given the thermal stratification of the water column. With rates of wave notch growth and ram face melt, we can estimate the growth of the ram as $V_{ram} = V_m - V_{rf}$. Mechanical failure of the ram depends on ram growth, yet ram growth is slowed by melting of ice at the sidewall. This leads to the interesting result that melting at the vertical face actually acts to *slow* the overall rate of lateral deterioration associated with footloose calving.

A.4. Ram Calving

Wagner et al. (2014) found that the critical ram length at which failure will occur (L_{crit}) is,

$$L_{crit} = \frac{e^{\frac{\pi}{4}} \rho_w h_T \sigma_F}{6 \rho_i L_w g (\rho_w - \rho_i)} \tag{A.5}$$

where ρ_w and ρ_I are the water and ice densities, g is acceleration due to gravity, σ_F is a failure stress (the tensile stress in the extreme fibre that will result in ice failure), and h_T is the total thickness of the ice island. We do not consider the height of the wave notch, assuming that the extension of the wave notch below the mean sea surface is much smaller than the draft of the ice island. The characteristic length (L_w) is,

$$L_w = \left[\frac{E {h_T}^3}{12(1-\nu^2)\rho_w g} \right]^{1/4} \tag{A.6}$$

where E is an effective Young's modulus, and ν is Poisson's ratio. The ice island length must be substantially greater than L_w for the upward buoyancy-driven force to result in bending and failure through the footloose mechanism. An assessment of ice island length and imposed stress is detailed in Section 3 along with information regarding the filtering of ice island branches, imposed for our study, based on the length dimension. Our assignment of E (1 GPa) is informed by past geophysical studies (Vaughan, 1995; Wagner et al., 2014). This assignment is less than the Young's modulus of pure and undamaged ice given the heterogenous density and small-scale damage of ice in non-laboratory settings. It is an effective value that better captures ice bending characteristics at very large scales. Using a value of 10 GPa in our default case would result in about a 45 % decrease in the time to failure, and 75 % increase in the average erosion rate.

The failure stress ($\sigma_F = 200$ kPa) was also selected to be appropriate at ice island scales given the values used and discussed in previous work (Robe, 1980; Wagner et al., 2014). The time to failure is a linear function of failure stress. Doubling σ_F would double the time to failure. The effect on average erosion rate is non-linear, but using our default values with an increased failure stress value of 400 kPa would decrease the average lateral erosion rate by about 50 %.

After combining (A.5) and (A.6) we can define a parameter (γ) containing variables that can be considered constant,

$$\gamma = \frac{e^{\frac{\pi}{4}} \rho_w [12(1-\nu^2)\rho_w g]^{1/4}}{6 \rho_i g (\rho_w - \rho_i)} \tag{A.7}$$

leaving,

$$L_{crit} = \gamma \sigma_F \left[\frac{h_T}{E} \right]^{1/4}. \tag{A.8}$$

We see that L_{crit} is a linear function of the critical stress, but only weakly dependent on thickness and Young's modulus. Failure will then occur at the point of maximum stress (x_{max}), this distance being along the axis running perpendicular to the ice edge and into the center of the ice island,

$$x_{max} = \frac{\pi}{4\beta} \tag{A.9}$$

We note that the presented beam equations assume that the ice material extends to infinity in the x-direction away from the free face. The distance between the wave notch and x_{max} is approximately the same as L_w (Wagner et al., 2014). The parameter β has units of m^{-1} and is related to the characteristic length L_w as $\beta = 2^{(-1/2)}L_w^{-1}$. It determines the amplitude of the deformation from bending and is calculated from,

$$\beta = \left[\frac{\rho_w g}{4D}\right]^{1/4} \tag{A.10}$$

where the flexural rigidity D is,

$$D = \frac{Eh_T^3}{12(1-\nu^2)} \tag{A.11}$$

(e.g., Watts, 2002). The buoyancy from the ram is calculated as a vertical load per unit width (P_1) applied at the free end of the beam (minus the ram),

$$P_1 = L_{ram} h_K (\rho_w - \rho_i) g\,. \tag{A.12}$$

The beam thickness is the full thickness of the ice island (h_T), which in our simulations is constant. The keel (and ram) thickness is calculated from buoyancy,

$$h_K = h_T - h_T \cdot (\rho_w - \rho_i)/\rho_w \tag{A.13}$$

(Wagner et al., 2014). The deflection (y_x), bending moment (M_x), and stress (σ_x) are calculated from Eqs. A14 – A16:

$$y_x = \frac{2P_1\beta}{\rho_w g} \cdot exp[-\beta x] \cdot cos[\beta x] \tag{A.14}$$

$$M_x = \frac{P_1}{\beta} \cdot exp[-\beta x] \cdot sin[\beta x] \tag{A.15}$$

$$\sigma_x = \frac{E}{(1-\nu^2)} \cdot \frac{2P_1\beta^3 h}{\rho_w g} \cdot exp[-\beta x] \cdot sin[\beta x] \tag{A.16}$$

(Hetenyi, 1946; Watts, 2002). The maximum stress, σ_{max}, at x_{max} has magnitude (Watts, 2002)

$$\sigma_{\max} = \frac{E}{(1-\nu^2)} \frac{2P_1\beta^3 h_T}{\rho_w g} \cdot exp[-\pi/4] \cdot sin[\pi/4] \tag{A.17}$$

The extension of the ram beyond the end of the beam will result in a small force due to the moment. Like Wagner et al. (2014), we ignore it. Fig. A.2 shows the deflections, moments, and stresses derived from the preceding formulations and the base-case parameters from Table 1. The base-case value for L_{crit} is 21.4 m and x_{max} is 319 m.

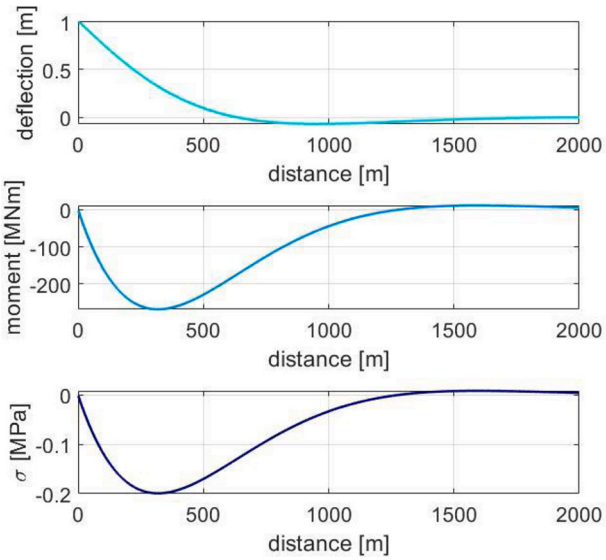

Fig. A.2. Deflection (top), bending moment (middle) and stress (bottom) with increasing distance from the ice island edge as calculated with the default values from Table 1.

Appendix B. Symbols used in this article

τ	Wave period (s)
Γ	Latent heat of melting (J kg^{-1})
ρ_i	Sea water density (kg m^{-3})
ρ_w	Ice density (kg m^{-3})
ν	Poisson's ratio
ν_w	Water viscosity (m^2 s^{-1})
σ_F	Failure stress (kPa)
σ_{max}	Maximum stress (MPa)
a	Empirical constant ($^\circ C^{-1}$)
c	Bulk heat transfer coefficient ($m^{0.4}$ $s^{-0.2}$ $^\circ C^{-1}$)
C^+	Enhanced lateral erosion coefficient
D	Flexural rigidity (Pa m^4)
E	Effective Young's modulus (GPa)
g	Acceleration due to gravity (m s^{-2})
H	Wave height (m)
h_T	Ice island total thickness (m)
h_K	Ice island keel thickness (m)
K	Coefficient representing the average proportion of the total length of the ice island involved in a footloose calving event
k	Wave number (m^{-1})
k_w	Thermal conductivity of sea water (W m^{-1} $^\circ C$)
L	Extreme ice island water line length (m)
L_{crit}	Critical ram length at which failure will occur (m)
L_f	Length of an ice face (m)
L_{ram}	Ram length, distance from wave notch to the outer face of a ram (m)
L_w	Characteristic length or buoyancy length. Distance from the wave notch to the point of failure (m)
Pr	Prandtl Number
P_1	Vertical load per unit width (kg s^{-2})
r	Length to width ratio
$Re_H(z)$	Depth-dependent wave Reynolds number
ΔT	Difference between far field ocean surface temperature and ice melting temperature ($^\circ C$)
T_f	Seawater freezing temperature ($^\circ C$)
T_m	Ice melting temperature ($^\circ C$)
T_∞	Far field ocean surface temperature ($^\circ C$)
u	Differential ice/water velocity (m s^{-1})
V_m	Wave-induced melt rate, rate of notch growth (m s^{-1})
V_{ram}	Rate of ram growth (m s^{-1})
V_{rf}	Melt rate of the outer ram face (m s^{-1})
W	Width (m)
W_F	Failure width (m)
x_{max}	Point of maximum stress (m)
z	Depth (m)

References

Barnhart, K., Anderson, R., Overeem, I., Wobus, C., Clow, G., Urban, F., 2014. Modeling erosion of ice-rich permafrost bluffs along the Alaskan Beaufort Sea coast. J. Geophys. Res. Earth 119, 1155–1179. https://doi.org/10.1002/2013JF002845.

Becker, M.K., Howard, S.L., Fricker, H.A., Padman, L., Mosbeux, C., Siegfried, M.R., 2021. Buoyancy-driven flexure at the front of Ross Ice Shelf, Antarctica, observed with ICESat-2 laser altimetry. Geophys. Res. Lett. 48, e2020GL091207. https://doi.org/10.1029/2020GL091207.

Benn, D.I., Åström, J., Zwinger, T., Todd, J., Nick, F.M., Cook, S., Hulton, N.R.J., Luckman, A., 2017. Melt-under-cutting and buoyancy-driven calving from tidewater glaciers: new insights from discrete element and continuum model simulations. J. Glaciol. 63, 691–702. https://doi.org/10.1017/jog.2017.41.

Bigg, G., Wadley, M., Stevens, D., Johnson, J., 1997. Modeling the dynamics and thermodynamics of icebergs. Cold Reg. Sci. Technol. 26, 113–135. https://doi.org/10.1016/S0165-232X(97)00012-8.

Bruneau, S., Manning, E., Crocker, G., 2011. The Incorporation of an Ocean Temperature Profile into an Existing Iceberg Deterioration Model. Proceedings of the 21st International Conference on Port and Ocean Engineering under Arctic Conditions. 10–14 July, Montréal, Canada. POAC11–114.

Canadian Ice Service, 2005. MANICE: Manual of Standard Procedures for Observing and Reporting Ice Conditions (Rev. 9th ed.). Environment Canada, Ottawa. Date of access: 23 January 2024. https://www.canada.ca/en/environment-climate-change/services/weather-manuals-documentation/manice-manual-of-ice.html.

Copernicus Climate Change Service (C3S), 2017. ERA5: Fifth generation of ECMWF atmospheric reanalyses of the global climate. In: Copernicus Climate Change Service Climate Data Store (CDS). Date of access: 2 July 2023. https://cds.climate.copernicus.eu/cdsapp#!/home.

Crawford, A., Mueller, D., 2023. Assessing ice island drift patterns, ice island grounding locations, and gridded bathymetry products between Nares Strait and the North Atlantic. Arctic 76, 1–13. https://doi.org/10.14430/arctic76227.

Crawford, A., Mueller, D.R., Humphreys, E., Carrieres, T., Tran, H., 2015. Surface ablation model evaluation on a drifting ice island in the Canadian Arctic. Cold Reg. Sci. Technol. 110, 170–182. https://doi.org/10.1016/j.coldregions.2014.11.011.

Crawford, A.J., Wadhams, P., Wagner, T.J.W., Stern, A., Abrahamsen, E.P., Church, I., Bates, R., Nicholls, K.W., 2016. Journey of an Arctic ice island. Oceanography 29 (2), 254–263.

Crawford, A.J., Crocker, G., Mueller, D., Desjardins, L., Saper, R., Carrieres, T., 2018a. The Canadian Ice Island Drift, Deterioration and Detection (CI2D3) Database. Journal of Glaciology 64 (245), 517–521. https://doi.org/10.1017/jog.2018.36.

Crawford, A.J., Mueller, D., Desjardins, L., Myers, P.G., 2018b. The aftermath of Petermann Glacier calving events (2008-2012): Ice island size distributions and meltwater dispersal. J. Geophys. Res. Oceans 123 (12), 8812–8827. https://doi.org/10.1029/2018JC014388.

Crawford, A.J., Mueller, D., Crocker, G., Mingo, L., Desjardins, L., Dumont, D., Babin, M., 2020. Ice island thinning: rates and model calibration with in situ observations from Baffin Bay, Nunavut. The Cryosphere 14, 1067–1081. https://doi.org/10.5194/tc-14-1067-2020.

Crocker, G., 2001. Analysis of iceberg model verification data collected in June 2001. Contract Report Prepared for Canadian Ice Service. Ballicater Consulting Ltd.. Report 01–05.

Crocker, G., 2003. Analysis of Iceberg Model Verification Data Collected to May 2002, Contract Report for Canadian Ice Service. Ballicater Consulting Ltd. (Report 03-1.).

Crocker, G., 2012. Ice island and iceberg studies 2012. In: Contract Report Prepared for Canadian Ice Service, Ballicater Consulting Ltd., Report 12–01.

Crocker, G., Carrieres, T., Tran, H., 2013. Ice Island Drift and Deterioration Forecasting in Eastern Canada. Proceedings of the 22nd International Conference on Port and Ocean Engineering under Arctic Conditions. 9–13 June, Espoo, Finland. POAC13–166.

Desjardins, L., Crawford, A., Mueller, D., Saper, R., Schaad, C., Stewart-Jones, E., Shepherd, J., 2018. Canadian Ice Island Drift, Deterioration and Detection Database (CI2D3 Database) [v1.1]. Canadian Cryospheric Information Network (CCIN), Waterloo, Canada. https://doi.org/10.21963/12678.

Diemand, D., 1987. On the splitting of icebergs natural and induced. In: Proceedings of the 6th International Offshore Mechanical and Arctic Engineering Symposium. 1-6 March, Houston, USA, pp. 1–9.
England, M.R., Wagner, T.J.W., Eisenman, I., 2020. Modeling the breakup of tabular icebergs. Science Advances 6, eabd1273. https://doi.org/10.1126/sciadv.abd1273.
Fenz, D., Kokkinis, T., 2012. Loads on downward breaking cones from managed ice floes. In: Proceedings of the SNAME 10th International Conference and Exhibition on Performance of Ships and Structures in Ice. 17-20 September, Banff, Canada. SNAME-ICETECH-2012-154. https://doi.org/10.5957/ICETECH-2012-154.
Fuglem, M., Jordaan, I., 2017. Risk Analysis and Hazards of Ice Islands. In: Mueller, D., Copland, L. (Eds.), Ice Shelves and Ice Islands of the Canadian Arctic. Springer, New York, New York, USA, pp. 395–415.
Fuglem, M., Richard, M., Kennedy, A., King, T., Cater, N., 2012. Modeling risks to offshore facilities associated with ice islands off Canada's East Coast. In: Proceedings of ICETECH 2012, International Conference on Performance of Ships and Structures in Ice. 17-20 September, Banff, Canada. ICETECH12-137-R0.
Gladstone, R., Bigg, G., Nicholls, K., 2001. Iceberg trajectory modeling and meltwater injection in the Southern Ocean. J. Geophys. Res. 106 (C9), 19903–19915. https://doi.org/10.1029/2000JC000347.
Goodman, D.J., Wadhams, P., Squire, V.A., 1980. The flexural response of a tabular ice island to ocean swell. Ann. Glaciol. 1, 23–27.
Hetenyi, M., 1946. Beams on Elastic Foundations: Theory with Applications in the Fields of Civil and Mechanical Engineering. University of Michigan Press, Ann Arbor, Michigan, USA.
The dynamics of iceberg grounding and scouring (DIGS) experiment and repetitive mapping of the eastern Canadian continental shelf. In: Hodgson, G., Lever, J., Woodworth-Lynas, C., Lewis, C. (Eds.), 1988. Environmental Studies Research Funds Report No. 094.
Huth, A., Adcroft, A., Sergienko, O., 2022a. Parameterizing tabular-iceberg decay in an ocean model. Journal of Advances in Modeling Earth Systems 4, e2021MS002869. https://doi.org/10.1029/2021MS002869.
Huth, A., Adcroft, A., Sergienko, O., Khan, Z., 2022b. Ocean currents break up a tabular iceberg. Science Advances 8 (42)), eabq6974. https://doi.org/10.1126/sciadv.abq6974.
Kobayashi, N., 1985. Formation of thermoerosional niches into frozen bluffs due to storm surges on the Beaufort Sea coast. J. Geophys. Res. 90 (C6), 11,983–11,988.
Kubat, I., Sayed, M., Savage, S.B., 2005. An operational model of iceberg drift. International Journal of Offshore and Polar Engineering 15 (2), 125–131. JC-372.
Kubat, I., Sayed, M., Savage, S., Carrieres, T., Crocker, G., 2007. An operational iceberg deterioration model. In: Proceedings of the 16th International Offshore and Polar Engineering Conference. 1-6 July, Lisbon, Portugal. Paper 2007-JSC-409, 2007-07-01.
Løset, S., 1993. Numerical modeling of the temperature distribution in tabular icebergs. Cold Reg. Sci. Technol. 21, 103–115.
Marson, J., Gillard, L., Myers, P., 2021. Distinct Ocean responses to Greenland's liquid runoff and iceberg melt. J. Geophys. Res. Oceans 126 (12). https://doi.org/10.1029/2021JC017542.
Martin, S., Joseberger, J., Kauffman, P., 1978. Wave-induced heat transfer to an iceberg. In: Husseiny, A. (Ed.), Iceberg Utilization. Proceedings of a Conference held at Iowa State University. 2–6 October 1977. Pergammon Press, Ames, USA, pp. 260–264.
Merino, N., Le Sommer, J., Durand, G., Jourdain, N.C., Madec, G., Mathiot, P., Tournadre, J., 2016. Antarctic icebergs melt over the Southern Ocean: Climatology and impact on sea ice. Ocean Modeling 104, 99–110. https://doi.org/10.1016/j.ocemod.2016.05.001.
Morrison, J., Goldberg, D., 2012. A brief study on the force balance between a small iceberg, the ocean, sea ice, and atmosphere in the Weddell Sea. Cold Reg. Sci. Technol. 76-77, 69–76. https://doi.org/10.1016/j.coldregions.2011.10.014.
Mosbeux, C., Wagner, T., Becker, M., Fricker, H., 2020. Viscous and elastic buoyancy stresses as drivers of ice-shelf calving. Journal of Glaciology 66 (258), 643–657. https://doi.org/10.1017/jog.2020.35.
Motz, E., 2022. Analysis of Iceberg Deterioration and Drift Using NAIS 2.0 (MSc Thesis). Naval Postgraduate School, Monterey, USA.
Neter, J., Kutner, M.H., Nachtsheim, C.J., Wasserman, W., 1996. Applied Linear Statistical Models, 4th ed. WCB McGraw-Hill, New York, New York, USA.
O'Leary, M., Christoffersen, P., 2013. Calving on tidewater glaciers amplified by submarine frontal melting. The Cryosphere 7, 119–128. https://doi.org/10.5194/tc-7-119-2013.
Reeh, N., 1968. On the calving of ice from floating glaciers and ice shelves. Journal of Glaciology 50, 215–232.
Robe, R.Q., 1980. Iceberg Drift and Deterioration. In: Colbeck, S.C. (Ed.), Dynamics of Snow and Ice Masses. Academic Press, New York, New York, USA, pp. 211–258.
Sartore, N.B., Wagner, T.J.W., Siegfried, M.R., Pujara, N., Zoet, L.K., 2024. Calving of Ross Ice Shelf from wave erosion and hydrostatic stresses. Cryosphere Discuss. https://doi.org/10.5194/egusphere-2024-571. EGUsphere [preprint].
Sazidy, M., Crocker, G., Mueller, D., 2019. A 3D Numerical Model of Ice Island Calving Due to Buoyancy-Driven Flexure. Proceedings of the 25th International Conference on Port and Ocean Engineering under Arctic Conditions. 9–13 June, Delft, The Netherlands. POAC19–008.
Scambos, T., Sergienko, O., Sargent, A., MacAyeal, D., Fastook, J., 2005. ICESat profiles of tabular iceberg margins and iceberg breakup at low latitudes. Geophys. Res. Lett. 32, L23S09. https://doi.org/10.1029/2005GL023802.
Slater, D.A., Benn, D.I., Cowton, T.R., Bassis, J.N., Todd, J.A., 2021. Calving multiplier effect controlled by melt undercut geometry. J. Geophys. Res. Earth 126, e2021JF006191. https://doi.org/10.1029/2021JF006191.
Smith, J., 2020. Modeling Ice Island Calving Events with Finite Element Analysis (MSc thesis) Carleton University, Department of Geography and Environmental Studies, Ottawa, Canada 90 pp. https://doi.org/10.22215/etd/2020-13905.
Stern, A.A., Johnson, E., Holland, D.M., Wagner, T.J.W., Wadhams, P., Bates, R., Abrahamsen, E.P., Nicholls, K.W., Crawford, A., Gagnon, J., Tremblay, J.-E., 2015. Wind-driven upwelling around grounded tabular icebergs. J. Geophys. Res. Oceans 120 (8), 5820–5835. https://doi.org/10.1002/2015JC010805.
Trevers, M., Payne, A.J., Cornford, S.L., Moon, T., 2017. Buoyant forces promote tidewater glacier iceberg calving through large basal stress concentrations. Cryosphere 13 (7), 1877–1887. https://doi.org/10.5194/tc-13-1877-2019.
Turnbull, I.D., Fournier, N., Stolwijk, M., Fosnaes, T., McGonigal, D., 2015. Operational iceberg drift forecasting in Northwest Greenland. Cold Reg. Sci. Technol. 110, 1–18. https://doi.org/10.1016/j.coldregions.2014.10.006.
Vaughan, D.G., 1995. Tidal flexure at ice shelf margins. J. Geophys. Res. Solid Earth 100, 6213–6224. https://doi.org/10.1029/94JB02467.
Wagner, T.J.W., Eisenman, I., 2017. How climate model biases skew the distribution of iceberg meltwater. Geophys. Res. Lett. 44 (8), 3691–3699. https://doi.org/10.1002/2016GL071645.
Wagner, T.J.W., Wadhams, P., Bates, R., Elosegui, P., Stern, A., Vella, D., Abrahamsen, E., Crawford, A., Nicholls, K., 2014. The "footloose" mechanism: iceberg decay from hydrostatic stresses. Geophys. Res. Lett. 41, 5522–5529. https://doi.org/10.1002/2014GL060832.
Wagner, T.J.W., James, T.D., Murray, T., Vella, D., 2016. On the role of buoyant flexure in glacier calving. Geophys. Res. Lett. 43, 232–240A. https://doi.org/10.1002/2015GL067247.
Wagner, T.J.W., Dell, R., Eisenman, I., 2017. An analytical model of iceberg drift. J. Phys. Oceanogr. 47, 1605–1616. https://doi.org/10.1175/JPO-D-16-0262.1.
Watts, A.B., 2002. Isostacy and Flexure of the Lithosphere. Cambridge University Press, 458 pp.
Weeks, W., Campbell, W., 1973. Icebergs as a freshwater source: an appraisal. Journal of Glaciology 12, 207–233.
White, F., Spaulding, M., Gominho, L., 1980. Theoretical estimates of the various mechanisms involved in iceberg deterioration in the open ocean. In: US Coast Guard Report CG-D-62-80.